Test Results of a Twin-rotor Radial-inflow Self-rectifying Air Turbine for OWC Wave Energy Converters

Bárbara Sofia C. Lopes
barbara.lopes@tecnico.ulisboa.pt

Instituto Superior Técnico, Universidade de Lisboa, Portugal

November 2017

Abstract

The paper reports an experimental study of a self-rectifying twin-rotor air turbine to be installed in an oscillating water column wave energy converter. The turbine is based on a pair of conventional radial-inflow rotors mounted on a common shaft, complemented by the corresponding inlet guide vane rows, by a curved-duct manifold arranged circumferentially in a periodic manner and by a two-position axially-moving cylindrical valve. The valve ensures that the air flows alternately through one or the other of the two parts of the twin-rotor turbine, depending on the sign of the pressure head. For this reason, only one half of the turbine was constructed. It was tested in unidirectional flow at the blow-down test rig of Instituto Superior Técnico.

Keywords: Wave energy, oscillating water column, air turbine, twin-rotor self-rectifying turbine, experimental results.

1. Introduction

The oscillating water column (OWC) is the simplest type of wave energy converter. The OWC can be integrated into a breakwater, isolated or in a floating configuration (Fig. 1) and its success depends on the performance and reliability of the air turbine. It is equipped with an air turbine, usually a self-rectifying turbine, which is a turbine whose rotational direction is independent of the flow direction with no need of a check valve system. The best known types of self-rectifying turbines are the Wells turbine and the impulse turbine, with axial-flow and radial-flow variants of both (see [1, 2]). The efficiency of the Wells turbine is limited by the aerodynamic conception of the turbine itself. Impulse turbines are characterized by substantial aerodynamic losses at the second row of guide vanes (see [3]).

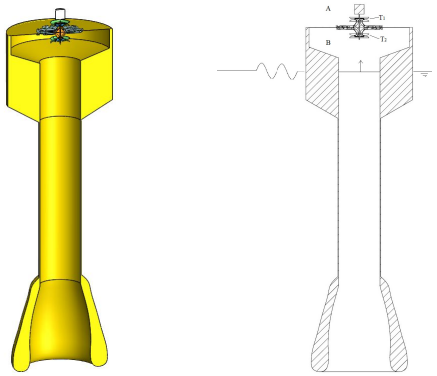

a) b)

Fig. 1: a) Section view of OWC and b) schematic view of OWC.

The twin-rotor turbine appears from the idea of associating two identical "conventional" air turbines T_1 and T_2. The two turbines can be coupled to a common electrical generator or, alternately, each turbine is coupled to its own generator. The efficiency of the twin unidirectional turbine topology is negatively affected by one of the twin turbines absorbing a non-insignificant part of the total flow while consuming some power from the generator (due to negative torque). A novel twin-rotor turbine was patented in 2015 [4] and is described in [5]. The innovative part of this twin-rotor turbine is its diffusor shaped as a curved-duct manifold complemented with a cylindrical two- or three-position axially-moving valve.

The object of this paper is the experimental study of the twin-rotor turbine. The twin-rotor radial-inflow configuration is presented in section 2. Section 3 describes the experimental set-up, namely the turbine model and the test rig. The following section presents the experimental results. Finally, section 5 deals with the conclusions and suggestions for future work.

2. The twin-rotor radial-inflow turbine

The turbine has two sets of radial-inflow rotor blades mounted on a common shaft and axially offset from

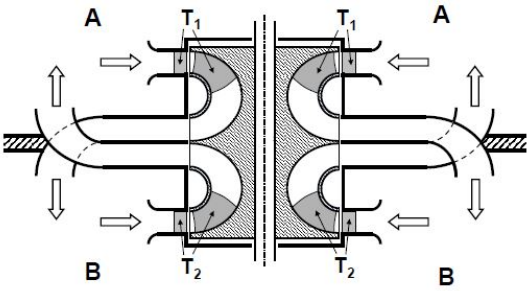

Fig. 2: New turbine with twin radial-inflow rotors (reproduced from [5]).

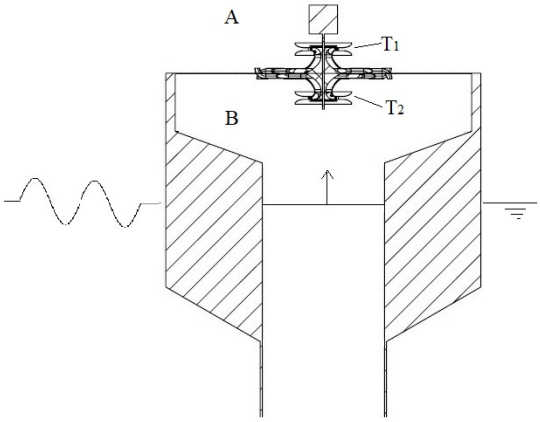

Fig. 3: Detailed view of Fig. 1 b).

each other. Each set of rotor blades is complemented by a set of guide vanes, as in a conventional unidirectional turbine. This whole set of rotor blades and guide vanes may be regarded as forming two conventional single-stage radial inflow gas turbines, T_1 and T_2, Fig. 2.

The turbine operates between spaces A (atmosphere) and B (pneumatic chamber), respectively at pressures p_A and p_B (see Figs. 2 and 3). When $p_A > p_B$ the air flows through turbine T_1; conversely, when $p_A < p_B$ the air flows through turbine T_2. This is made possible by a double set of curved ducts arranged circumferentially and alternately open to space A and B. Each rotor is connected to the corresponding set of curved ducts by a vaneless bladeless space bounded by curved and plane walls of revolution, as shown in Fig. 4. The radial extent of this bladeless space allows it to act as a diffuser, recovering part of the kinetic energy at rotor exit before flow entrance into the curved-duct manifold.

The configuration of the new turbine makes it possible to install a two-position axially-sliding valve, that is operated to prevent air from flowing in the reverse direction, Fig. 5. If a three-position axially-sliding valve is installed, then air can be prevented from flowing between spaces A an B, which means stopping the flow through both rotors to achieve latching, Fig. 6.

A model of the twin-rotor radial-inflow turbine was designed, constructed and tested at Instituto Superior

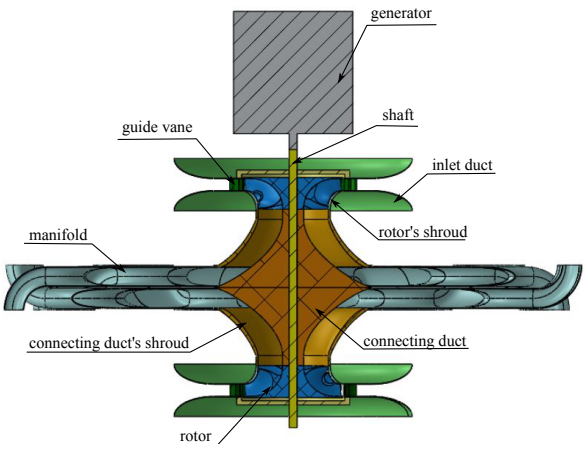

Fig. 4: Twin-rotor radial-inflow air turbine section view.

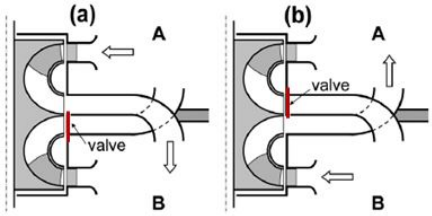

Fig. 5: Two-position axially-sliding valve (adapted from [5]).

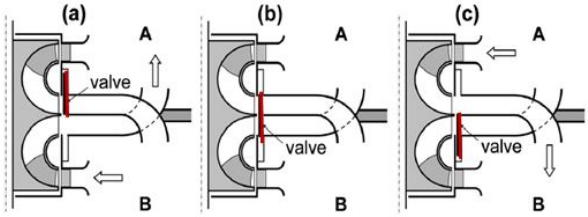

Fig. 6: Three-position axially-sliding valve (adapted from [5]).

Técnico (IST), Lisbon, as one of the tasks of the WET-FEET project, funded by the European Commission under program H2020.

The twin-rotor turbine consists of two identical parts, with two sets of curved ducts intertwined with each other. For this reason, only one half of the turbine was constructed and tested in unidirectional flow in the blow-down test rig of IST.

3. Experimental set-up

3.1. Turbine model

The rotor and the corresponding guide vanes are geometrically similar, and larger by a factor of 1.6, to a turbine of high efficiency designed for incompressible flow and studied in detail in [6].

The rotor (Fig. 7) has 17 blades with double curvature. The 17 rotor blades were made of Al 7075 and were

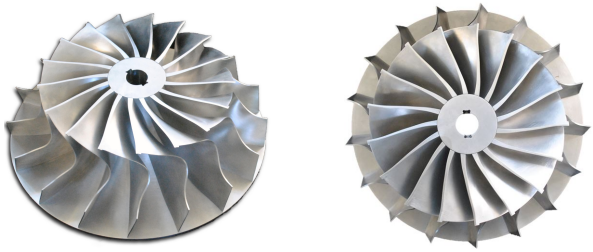

(a) (b)

Fig. 7: The turbine rotor.

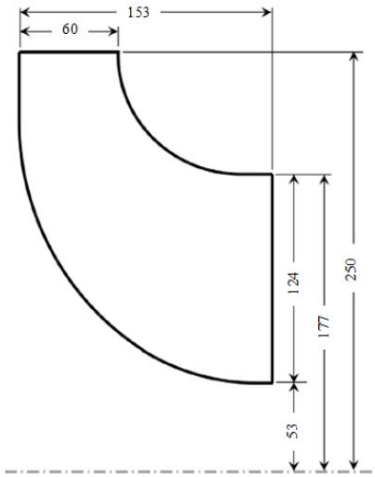

Fig. 8: Main dimensions of the turbine rotor (in mm).

machined in a 5-axis CNC machine – this manufacturing process was mandatory to ensure the required blade tolerances. Rotor dimensions are given in Fig. 8.

The 31 guide vanes are responsible for deflecting the air from a radial direction to a direction almost tangential, which is necessary, because the air is sucked radially through the turbine. The guide vanes were made of resin using a silicon mould and a master blade. The turbine shaft was made of AISI 1045 steel and was supported by three bearings (two ball bearings and one tapered roller bearing).

The relation between the rotor radius and the curved-duct manifold's entrance radius was selected based on information in [5] (see Fig. 9). In order to achieve high efficiency, a ratio R_4/R_2=1.5 was adopted. The optimization and geometrical design of the ducted manifold was done with the help of a CFD code, as described in [7]. The width at manifold entrance is b_4=94 mm. The curved duct manifold is composed of 9 equal ducts, Fig. 10. The total area of the exit sections is 9×0.0405=0.364 m^2. This should be compared with the annular area at rotor exit 0.0899 m^2, i.e., 4.05 times less. This shows that the diffusor should be capable of recovering most of the kinetic energy associated with the axial component of the velocity at rotor exit. Because of its radial extent, the diffusor should be expected to recover part of the kinetic

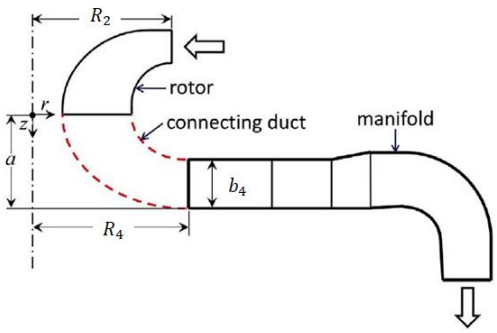

Fig. 9: Rotor, curved-duct manifold and axisymmetric connecting duct.

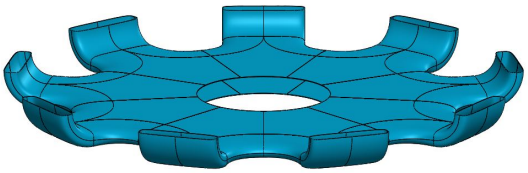

Fig. 10: Representation of the curved-duct manifold.

energy due to swirl at rotor exit.

The turbine manifold was manufactured of fiberglass. Due to its periodic geometry, the manifold was decomposed into several equal parts. An aluminium mould was produced for each of the parts. In the final assembly, these parts were joined by using an epoxy glue and bolts. The axisymmetric duct that connects the rotor to the curved-duct manifold was manufactured of Al 7075 with a 5-axis CNC machine. The duct is made of two parts assembled with threaded rods to reduce the machined material. The connecting duct shroud was manufactured in fiberglass using an Expanded PolyStyrene (EPS) and Polyvinyl Chloride (PVC) mould. The inlet ducts were made of fibre glass using a Medium Density Fiberboard (MDF) mould. The mould was filled with plaster in different steps in order to obtain the desired geometry.

3.2. Experimental apparatus

The layout of the test rig is presented in Fig. 11. Air is sucked radially into the turbine directly from the atmosphere. The air is discharged from the curved-duct manifold directly to the plenum chamber of the test rig. The plenum chamber contains a honeycomb lattice, whose function is to remove any swirl before the air enters into a calibrated nozzle, downstream of which there is a radial-flow fan. The turbine rotor was coupled to an electrical motor/generator whose rotational speed could be controlled. The pressure head across the turbine was provided by a conventional radial-flow fan driven by a 160 kW electrical motor whose rotational speed could be controlled. Figure 12 presents a photograph of the

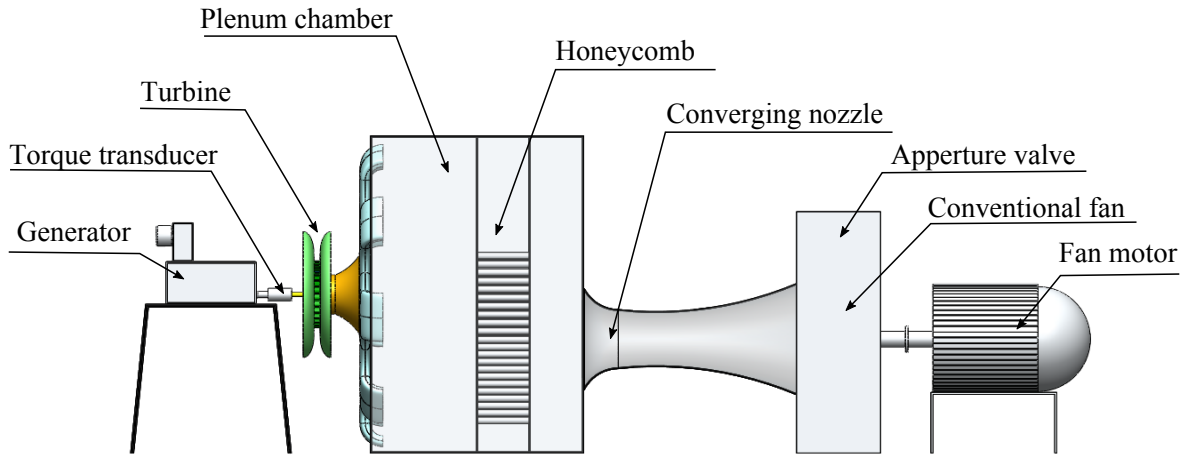

Fig. 11: Layout of the test rig at IST.

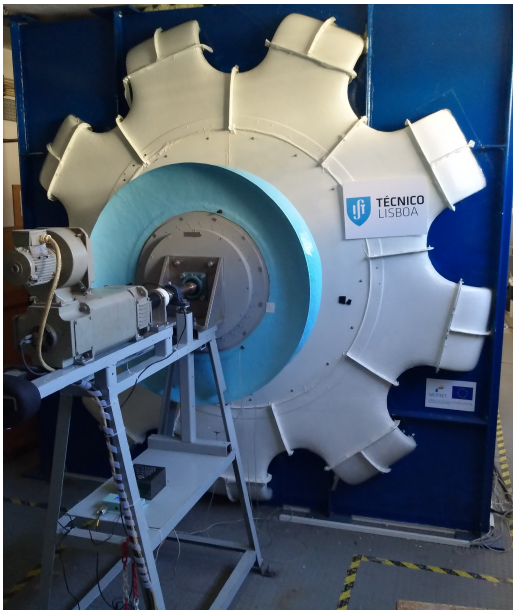

Fig. 12: Layout of the test rig, showing the electrical motor/generator, the inlet duct and the manifold.

test rig.

In order to evaluate the turbine performance, measurements were undertaken of volume flow rate, torque, rotational speed, temperature, humidity, pressure and atmospheric pressure. The volume flow rate was measured at the inlet to the guide vane system, at a radial distance of 77 mm upstream of the inlet guide vanes, from the static pressure relative to the atmosphere. The relation between the static pressure and the volume flow rate was obtained by calibration. The turbine shaft was connected to a Datum Electronics M425 Torque Transducer which gave the torque and the rotational speed. Temperature and humidity were measured using adequate sensors (LM 35 TO-92 and HIH-4000-001). Atmospheric pressure was measured using a Testo 511 – Absolute Pressure Meter. The other pressures were measured by pressure sensors of adequate range. Traverses were performed using a calibrated three-hole probe. The data acquisition system was National Instruments 6221 M series. All instruments were calibrated in order to convert the voltage (that appears in the data acquisition system) to the proper unit (e.g. convert voltage into pressure).

Special attention was taken to avoid air leaks in the circuit in order to have a constant flow. The air flow was assumed incompressible throughout the experiments.

4. Results

4.1. Turbine dimensionless numbers

The use of dimensionless variables has the advantage of extending the applicability of the results from the testing of a given machine to geometrically similar machines of different sizes, at various rotational speeds and with different fluid densities. We introduce the following dimensionless variables:

$$\Phi = \frac{Q}{\Omega D^3}, \tag{1}$$

$$\Pi = \frac{P}{\rho \Omega^3 D^5}, \tag{2}$$

$$\Psi = \frac{\Delta p}{\rho \Omega^2 D^2}. \tag{3}$$

Here Q is volume flow rate (m^3/s), D is rotor diameter (m), Ω is rotational speed (rad/s), P is turbine power output (W), ρ is air density (kg/m^3), Δp is pressure head between the atmosphere and the plenum chamber (Pa), Φ is dimensionless flow rate, Π is dimensionless power output and Ψ is dimensionless pressure head.

An important parameter in a turbine performance study is the turbine efficiency η. We define total-to-static efficiency, η, as

$$\eta = \frac{\Pi}{\Phi \Psi}. \tag{4}$$

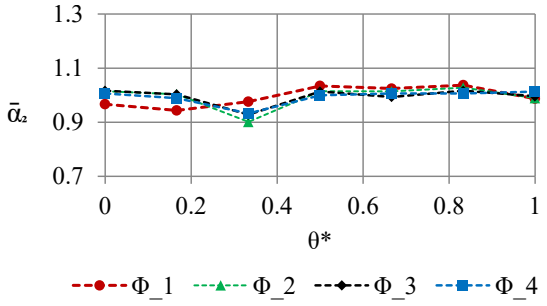

Fig. 13: Dimensionless plot of the velocity angle along the circumferential direction at rotor entrance.

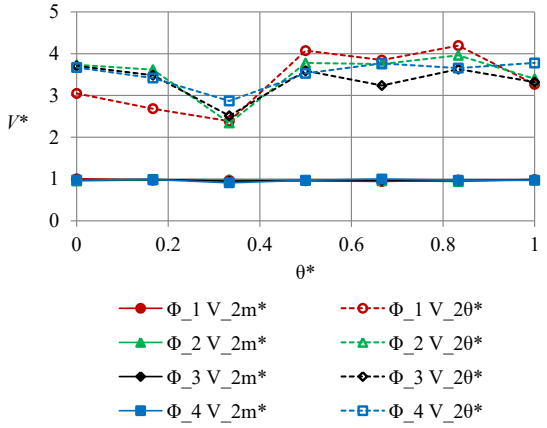

Fig. 14: Dimensionless velocity components along the circumferential direction for different flow rates at rotor entrance.

4.2. Rotor traverses

Detailed traverses were performed at rotor entrance and exit using a three-hole probe for four dimensionless flow rate coefficients: $\Phi_1 = 0.040$, $\Phi_2 = 0.050$, $\Phi_3 = 0.058$ and $\Phi_4 = 0.070$. It is important to have identical experimental conditions in the different traverses in order to analyse the results along the turbine. However this was difficult, because ambient conditions cannot be controlled and the rotational speed was controlled manually. The rotational speed during the traverses was maintained at 111 ± 1.57 rad/s.

Detailed traverses at rotor entrance were performed in the axial direction at 7 equally spaced circumferential stations so as to cover a complete angular pitch of the inlet guide vane row $360/31 = 11.6°$. The angle between two consecutive positions was 2°.

We define the normalized angle in the circumferential direction as $\theta^* = \theta/12°$.

Figure 13 shows the variation of the mean flow angle with the circumferential direction for the different flow rates. The mean flow angle, $\bar{\alpha}_2$, is defined as

$$\bar{\alpha}_2 = \frac{\arctan\left(\frac{\bar{V}_{2\theta}}{\bar{V}_{2\mathrm{m}}}\right)}{\arctan\left(\frac{\bar{V}_{2\theta}}{\bar{V}_{2\mathrm{m}}}\right)}, \tag{5}$$

where $\bar{V}_{2\theta}$ and $\bar{V}_{2\mathrm{m}}$ are, respectively, the mean meridional and the mean circumferential components of the velocity defined as

$$\bar{V}_{2\theta} = n_{\mathrm{blades}} \frac{\int_{z_1}^{z_2}\int_{\theta_0}^{\theta_{\mathrm{pitch}}} V_{2\theta} R_{2^*}\,\mathrm{d}\theta\mathrm{d}z}{\int_{z_1}^{z_2}\int_{0}^{2\pi} R_{2^*}\,\mathrm{d}\theta\mathrm{d}z}, \tag{6}$$

$$\bar{V}_{2\mathrm{m}} = n_{\mathrm{blades}} \frac{\int_{z_1}^{z_2}\int_{\theta_0}^{\theta_{\mathrm{pitch}}} V_{2\mathrm{m}} R_{2^*}\,\mathrm{d}\theta\mathrm{d}z}{\int_{z_1}^{z_2}\int_{0}^{2\pi} R_{2^*}\,\mathrm{d}\theta\mathrm{d}z}. \tag{7}$$

Here z is axial direction, θ is circumferential direction and n_{blades} is the number of rotor blades. Traverses were performed at radius $R_{2^*} = 0.257$ m.

Figure 13 shows that the mean angle depends on the circumferential coordinate but is almost independent of the volume flow rate. The determined mean angles, for the different circumferential coordinates, are very close to the angle of project ($\alpha_2 = 74°$).

Figure 14 presents the dimensionless velocity components $V^*_{2\mathrm{m}} = V_{2\mathrm{m}}/\bar{V}_{2\mathrm{m}}$ and $V^*_{2\theta} = V_{2\theta}/\bar{V}_{2\mathrm{m}}$ along the circumferential direction. Velocity components $V_{2\mathrm{m}}$ and $V_{2\theta}$ are defined as

$$V_{2\mathrm{m}} = \frac{\int_{\theta_1}^{\theta_2}\int_{b_1}^{b_2} V_{2\mathrm{m}}(b) R_{2^*}\,\mathrm{d}b\mathrm{d}\theta}{\int_{\theta_1}^{\theta_2}\int_{b_1}^{b_2} R_{2^*}\,\mathrm{d}b\mathrm{d}\theta}, \tag{8}$$

$$V_{2\theta} = \frac{\int_{\theta_1}^{\theta_2}\int_{b_1}^{b_2} V_{2\mathrm{m}}(b) V_{2\theta}(b) R_{2^*}\,\mathrm{d}b\mathrm{d}\theta}{\int_{\theta_1}^{\theta_2}\int_{b_1}^{b_2} V_{2\mathrm{m}}(b) R_{2^*}\,\mathrm{d}b\mathrm{d}\theta}. \tag{9}$$

Figure 14 shows that the meridional velocity component, $V^*_{2\mathrm{m}}$, is nearly independent of the volume flow rate and of the circumferential direction. Differently, the circumferential component, $V^*_{2\theta}$, varies with the circumferential coordinate and in some cases also with the volume flow rate. There is a negative peak in the circumferential component at $\theta^* = 1/3$.

The flow should be expected to be periodic in the circumferential direction. Figure 14 shows that the dimensionless velocity components are not exactly equal at $\theta^* = 0$ and at $\theta^* = 1$ due to experimental imprecision.

Rotor exit traverses were performed at a distance of 66 mm of the rotor exit due to space constraints. Figure 15 shows the angle variation along the radial direction and Fig. 16 presents the variation of the dimensionless velocity components along the spanwise direction. We define the angle at rotor exit, α^*_3, and the dimensionless velocity components, $V^*_{3\mathrm{m}}$ and $V^*_{3\mathrm{t}}$:

$$\alpha^*_3 = \arctan\left(\frac{V^*_{3\mathrm{t}}}{V^*_{3\mathrm{m}}}\right), \tag{10}$$

$$V^*_{3\mathrm{m}} = \frac{V_3 \cos\alpha_3}{\bar{V}_{3\mathrm{m}}}, \tag{11}$$

$$V^*_{3\mathrm{t}} = \frac{V_3 \sin\alpha_3}{\bar{V}_{3\mathrm{m}}}, \tag{12}$$

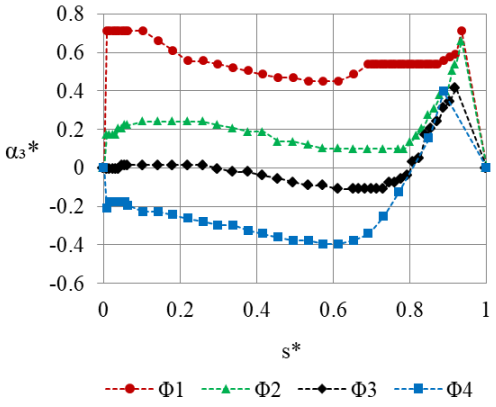

Fig. 15: Dimensionless plot of the velocity angle along the spanwise direction at rotor exit.

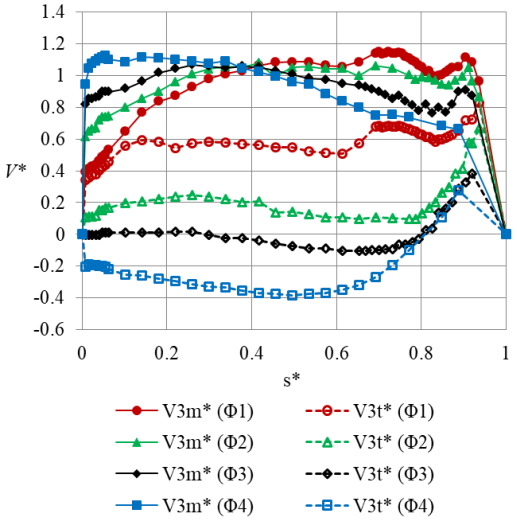

Fig. 16: Dimensionless velocity components along the spanwise direction for different flow rates at rotor exit.

$$\bar{V}_{3\mathrm{m}} = \frac{\int_{\theta_1}^{\theta_2}\int_{R_i}^{R_e} V_{3\mathrm{m}}^2(r) r \,\mathrm{d}r\mathrm{d}\theta}{\int_{\theta_1}^{\theta_2}\int_{R_i}^{R_e} V_{3\mathrm{m}} r \,\mathrm{d}r\mathrm{d}\theta}. \tag{13}$$

As expected, the angle can be positive or negative, depending on the flow rate coefficient, i.e. depending on the signal of the circumferential component of the velocity at rotor exit. At $s^* \approx 1$ we may see the influence of the hole through which the three-hole probe is introduced to perform the measurements.

Figure 16 shows that the meridional component of the velocity is always positive. The circumferential component can be positive or negative as anticipated before. We should expect to have minimum swirl at the flow rate coefficient, between Φ_2 and Φ_3, for which the efficiency is maximum. Not unexpectedly, even under peak efficiency conditions, the circumferential velocity component was found not to be exactly zero, which can be explained by the rotor blading geometrical design and

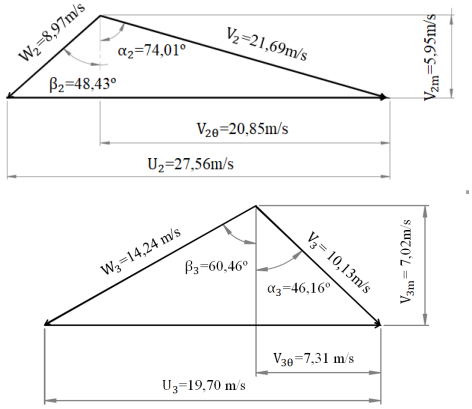

Fig. 17: Velocity diagram at entry to (subscript 2), and exit from (subscript 3), the rotor blades for $\Phi = 0.040$.

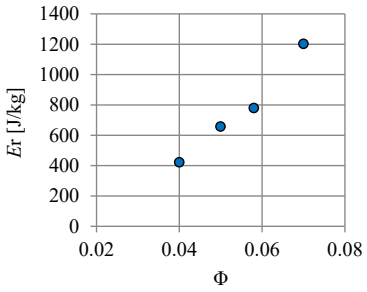

Fig. 18: Work done per unit mass, measured values.

also by the limited precision of the measurements.

The velocity triangles at entry to (subscript 2), and exit from (subscript 3) the rotor blades are plotted in Fig. 17 for $\Phi = 0.040$. Vector $\mathbf{U}$ is blade tip velocity ($U = \Omega D_{\mathrm{tip}}/2$), and vectors $\mathbf{V}$ and $\mathbf{W}$ are absolute and relative flow velocities, respectively. It is $U_2 \neq U_3$ because the velocity triangles correspond to different radii. As the passage area is different at entry to, and exit from, the rotor blades, it is $V_{2\mathrm{m}} \neq V_{3\mathrm{m}}$.

From Euler turbomachinery equation, we can determine the work done per unit mass:

$$E_{\mathrm{r}} = U_2 V_{2\theta} - U_3 V_{3\theta}. \tag{14}$$

Figure 18 shows the variation of the measured work done per unit mass with the volume flow rate. As expected, E_{r} increases with Φ.

4.3. Diffuser traverses

Due to space constraints, no pressure and velocity measurements could be done at the entrance to the curved-duct manifold, at radius $R_4 = 375\,\mathrm{mm}$. Instead, such measurements were performed at radius $R_{4^*} = 884\,\mathrm{mm}$ using a calibrated three-hole pressure probe; these measured results are identified by subscript 4. Traverses were performed along the axial direction between walls ($b^* = 0$ is the inlet wall and $b^* = 1$ is the

outlet wall, where a hole is located to allow the introduction of the probe for the measurements).

The angle of the velocity vector with the radial direction, at radius R_{4^*}, is defined as $\gamma = \arccos(V_{4r}/V_4)$. Its variation with the axial direction is presented in Fig. 19. The studied dimensionless flow rate coefficients are the same as at rotor's entrance traverses.

As expected, Fig. 19 shows that the flow angle, γ, can be positive or negative, depending on the flow rate coefficient; the signal of the angle is dependent on the signal of the circumferential component of the velocity.

4.4. Curved-duct and manifold performance

The diffusor shaped as a curved-duct manifold is the novel part of the twin-rotor turbine. In order to analyse the capacity of the connecting duct and the diffusor to recover the kinetic energy at rotor exit, we define the recovery coefficient ε_0:

$$\varepsilon_0 = \frac{p_B - p_3}{\frac{1}{2}\rho \bar{V}_3^2}, \tag{15}$$

here p_B and p_3 are the static pressure at the plenum chamber and at rotor exit, respectively. $\bar{V}_3$ is the average velocity at rotor exit determined by the ratio of volume flow rate and rotor exit area.

As seen in Fig. 20 the recovery coefficient reaches its maximum (0.914) at $\Phi = 0.05$. For a range $0.041 < \Phi < 0.075$, the coefficient exceeds 0.6, which means that in the indicated range, the connecting duct and the diffusor are recovering more than 60% of the kinetic energy associated with the axial flow velocity component at rotor exit. Naturally, if ε_0 were larger than unity, the recovered energy would also have to include part of the swirl velocity, associated to the circumferential component of the velocity.

4.5. Performance curves

The friction torque (for zero flow rate) has two components: aerodynamic and bearing losses; it is important to separately determine these components. The bearing losses are expected to be approximately independent of the rotational speed, while the aerodynamic losses or windage losses (for zero flow rate and large enough rotational speed) are expected to be proportional to the square of the rotational speed . Consequently, we expect the measured friction torque to be in the form $T_{\text{friction}} = a + b\Omega^2$. The variation of friction losses with the rotational speed is represented in Fig. 21. Interpolating the results by a polynomial with zero and second order terms, we can dedtermine both components

$$T_{\text{friction}} = 6.6585 \times 10^{-5}\Omega^2 + 0.7836. \tag{16}$$

The constant term represents the bearing torque whereas the second order term represents the aerodynamic loss torque (windage loss). The torque lost in bearings was added to the measured torque because it depends on the

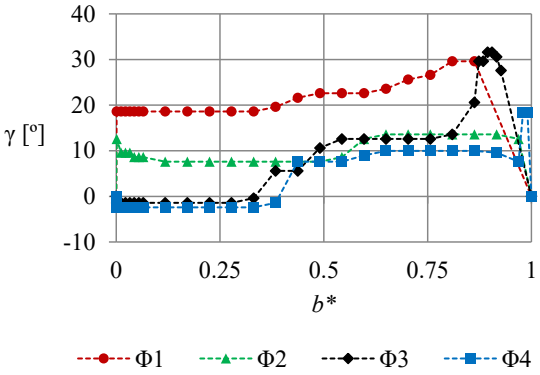

Fig. 19: Axial variation of velocity angle γ at radius R_{4^*}.

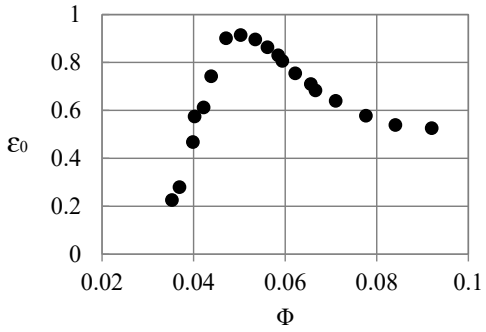

Fig. 20: ε_0 versus dimensionless flow coefficient.

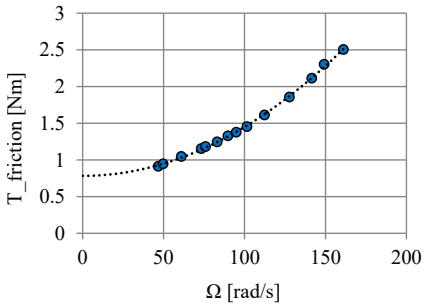

Fig. 21: Friction torque versus rotational speed.

installation and should not be regarded as an intrinsic characteristic of the turbine.

The twin-rotor turbine has two radial-inflow rotors mounted on a common shaft, as explained before. Both rotors are rotating at the same rotational speed but there is flow in only one. The passive rotor (the one without flow) is absorbing part of the energy. The amount of absorbed energy is dependent on rotational speed and corresponds to the aerodynamic losses (windage loss) determined previously. In the study of the performance of the twin-rotor turbine, the windage loss was subtracted from the measured power output of the turbine.

Figures 22 and 23 present, in the dimensionless form, turbine power output and the pressure head versus flow rate, respectively. The rotational speeds of the plotted results are between 74 and 137 rad/s. Both coefficients

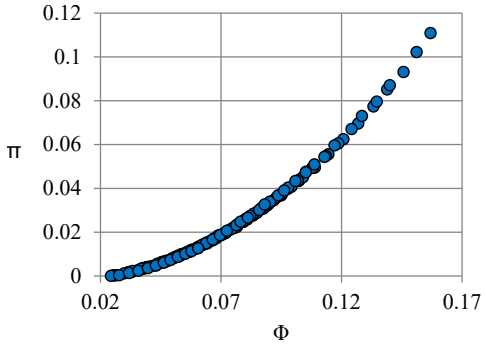

Fig. 22: Dimensionless twin-rotor turbine power output versus flow rate.

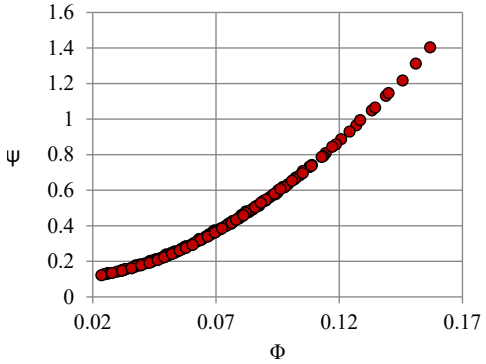

Fig. 23: Dimensionless twin-rotor turbine pressure head versus flow rate.

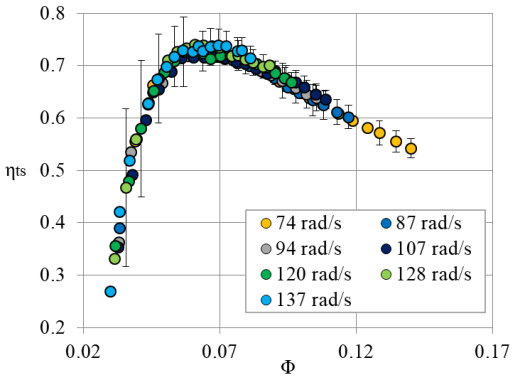

Fig. 24: Twin-rotor turbine efficiency versus flow rate.

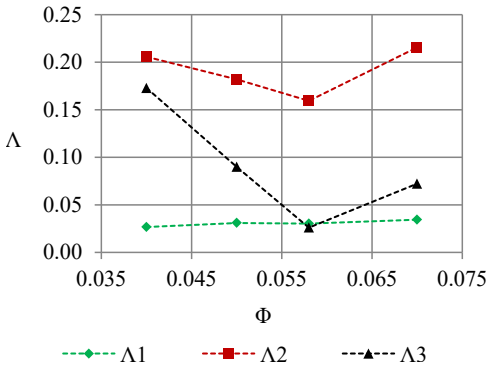

Fig. 25: Dimensionless plot of losses Λ versus flow rate

increase with flow rate. In contrast to axial-flow turbines (Wells or impulse), the pressure coefficient is non-zero at zero flow rate coefficient, as is usual in radial-flow rotors.

With the previous results, we plotted the twin-rotor turbine efficiency, Fig. 24. The maximum efficiency measured experimentally is 73.9% at $\Phi = 0.06$. Due to the passive rotor and its windage loss, the peak efficiency decreases by almost 12% relatively to the single turbine, i.e. half of the turbine, without the passive rotor. The uncertainty of the measurements is also represented in Fig. 24 [8]. As expected, the uncertainty decreases with the increase in flow rate.

4.6. Turbine losses

It is important to evaluate the losses along the turbine. The loss coefficient is defined as $\Lambda = p_{\text{loss}}/\Delta p$ where p_{loss} is pressure loss in units of pressure and Δp is the pressure head across the turbine. The losses between atmosphere and rotor entrance are represented by Λ_1; Λ_2 refers to rotor losses; Λ_3 accounts for losses between rotor exit and plenum chamber. It should be $\eta + \sum_{i=1}^{3} \Lambda_i = 1$. Figure 25 shows the losses for different flow rates. Λ_1 is nearly constant. As expected, rotor losses, Λ_2, are the most significant ones.

4.7. Performance in irregular waves

In real irregular waves, the twin-rotor turbine will operate under random pressure head conditions. Therefore, it is important to predict its average performance under such conditions. The stochastic model [9] was used to evaluate the twin-rotor turbine performance under irregular sea wave conditions. There are some assumptions when using the stochastic model: (i) waves are Gaussian processes and they are represented by a spectral distribution; (ii) linear water wave theory is applicable (small amplitude waves); (iii) the system is linear (Ψ/Φ=constant, constant rotational speed in a given sea state). As seen before, the turbine is non-linear (see Fig. 23). However, the use of stochastic modelling for non-linear systems is much more difficult and is out of the scope of this work. For this reason, the presented results should be seen as an approximation.

We define the averaged turbine efficiency as the ratio between the dimensionless average power output and the dimensionless average power available to the turbine, $\bar{\eta} = \bar{\Pi}/\bar{\Pi}_{\text{avai}}$. The average power output is given by

$$\bar{\Pi}(\sigma_\Psi) = \frac{1}{\sqrt{2\pi}\sigma_\Psi} \int_{-\infty}^{\infty} \exp\left(-\frac{\Psi^2}{2\sigma_\Psi^2}\right) \Pi(\Psi) \mathrm{d}\Psi, \quad (17)$$

where σ_Ψ is the dimensionless standard deviation or

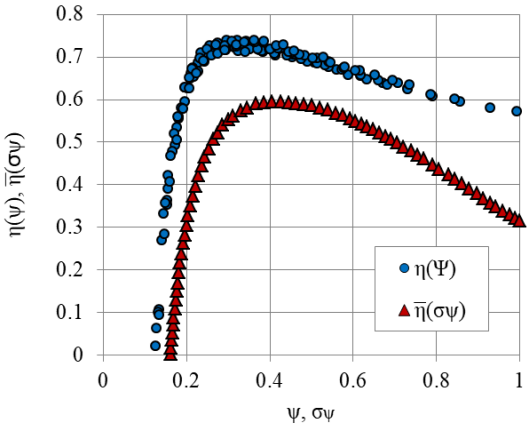

Fig. 26: Efficiency versus flow rate , $\eta(\Psi)$, and average efficiency in irregular waves versus rms of pressure head, $\bar{\eta}(\sigma_\Psi)$.

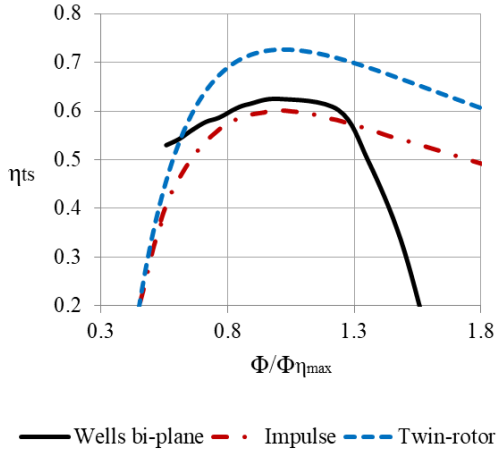

Fig. 27: Efficiency versus flow rate ratio $\Phi/\Phi_{\eta\max}$, where subscript $\eta_{\max}$ means maximum efficiency conditions.

root-mean-square of Ψ, Eq. (18),

$$\sigma_\Psi = \frac{\sigma_p}{\rho\Omega^2 D^2}, \tag{18}$$

and σ_p is the standard deviation of the pressure head Δp. The average available power output is

$$\bar{\Pi}_{\text{disp}}(\sigma_\Psi) = \frac{1}{\sqrt{2\pi}\sigma_\Psi}\int_{-\infty}^{\infty} \exp\left(-\frac{\Psi^2}{2\sigma_\Psi^2}\right)\Phi(\Psi)\Psi d\Psi, \tag{19}$$

where σ_Ψ^2 is the variance of Ψ. The curves (in dimensionless form) of $\Pi(\Psi)$ (power output versus pressure head) and $\Phi(\Psi)$ (flow rate versus pressure head) were obtained from experimental results. The averaged turbine efficiency is represented in Fig. 26. The efficiency curve obtained in laboratory experiments (permanent flow) is represented in the same figure.

The maximum averaged turbine efficiency is 59.9% for σ_Ψ=0.423. In order to achieve a maximum turbine average efficiency, the rotational speed should be controlled in such a way that σ_Ψ=0.423.

4.8. Comparison with other turbines

It is interesting to compare the twin-rotor turbine efficiency with other self-rectifying turbines commonly used in OWC. The most common air turbines for wave energy conversion are the axial-flow impulse turbine and the Wells turbine. Figure 27 presents the experimental efficiency curves for the twin-rotor turbine, for a bi-plane Wells turbine with guide-vanes between planes (see Ref. [10]) and for an axial-flow impulse turbine with pitching guide-vanes (see Ref. [3]).

The Wells bi-plane efficiency curve has a sharp drop, typical of this kind of turbines. Its maximum efficiency is 62.5%.

The maximum efficiency of the impulse turbine is about 60%, which is slightly below the peak efficiency of the Wells turbine. Unlike the Wells turbine, when the ratio $\Phi/\Phi_{\eta\max}$ increase above unity, the efficiency has a smooth decrease.

The efficiency of the twin-rotor turbine exceeds the efficiency of the other two turbines. Its peak efficiency is 73.9%. Like the impulse turbine, when $\Phi/\Phi_{\eta\max}$ increase above unity, the efficiency of the twin-rotor turbine decreases smoothly.

5. Conclusions

A new air turbine for bidirectional flow applications in wave energy conversion was experimentally investigated. The turbine is composed of two identical parts intertwined with each other; only half of the turbine was constructed and tested in unidirectional flow at the blow-down test rig of IST. The document presents experimental results for the single rotor and for the twin-rotor turbine. A main objective of this investigation was to study the recovered energy in the manifold diffuser, where flow velocity was found to be too small to be measured with the desired accuracy with the available equipment; this raised some problems. The turbine flow rate was measured at the turbine entrance, where the velocity was larger, rather than at the convergent-divergent nozzle downstream of the plenum chamber as usually done in previous tests of other types of turbines in the same test rig.

The flow angle and the velocity profiles were studied in detailed traverses at rotor entrance and exit, and also at the diffuser. The experimental results show that the curved-duct manifold and the connecting duct are able to recover most of the kinetic energy at rotor exit over a wide range of flow rates. The plot of the turbine pressure head coefficient versus the flow rate coefficient showed that, unlike Wells turbines, the tested twin-rotor turbine is clearly a non-linear turbine at constant rota-

tional speed. Bearing losses were determined and added to the measured turbine power output, as is reasonable to do. Windage losses at the passive rotor were also determined and found to significantly reduce the efficiency of the twin-rotor turbine.

The experimental results showed that the maximum efficiency of the twin-rotor turbine is 73.9% at a flow rate coefficient of 0.06. For the tested single-rotor turbine (without the passive rotor) the peak efficiency was found to be 86.6%. The difference, 12.7%, is due to the windage losses at the passive rotor. Windage losses are inherent to the twin-rotor turbine concept. Finding ways to reduce such losses by redesigning the rotor and/or its contruction method or by using a different type of rotor (possibly of axial-flow type) are important steps to improve the competitiveness of the twin-rotor type of turbine.

Performance comparisons with competing self-rectifying turbines show that the twin-rotor turbine clearly outperforms the biplane Wells turbine with guide vanes between planes and the axial-flow impulse turbine with pitching guide vanes.

Acknowledgements

This work was partially funded by the European Commission through the Horizon 2020 programme under agreement No. 641334, project WETFEET – "Wave Energy Transition to Future by Evolution of Engineering and Technology". The support of the Portuguese Foundation for the Science and Technology (FCT) through IDMEC, under LAETA Pest-OE/EME/LA0022 and PTDC/MAR-TEC/0914/2014, is also acknowledged.

References

[1] A. F. O. Falcão, L. M. C. Gato, Air turbines, in: A. Sayigh, editor. Comprehensive renewable energy, vol. 8, Ocean energy. Elsevier, (2012). p. 111–49. http:// dx.doi.org/10.1016/B978-0-08-087872-0.00805-2.

[2] A. F. O. Falcão, J. C. C. Henriques, Oscillating-water-column wave energy converters and air turbines: a review, Renew Energy 85, (2016) 1391–1424, http://dx.doi.org/10.1016/j.renene.2015.07.086.

[3] T. Setoguchi, S. Santhakumar, H. Maeda, M. Takao, K. Kaneko, A review of impulse turbines for wave energy conversion, Renew energy 23 (2) (2001) 261–292, http://dx.doi.org/10.1016/S0960-1481(00)00175-0.

[4] A. F. O. Falcao, L. M. C. Gato, J. C. C. Henriques, Air turbine for applications in wave energy conversion, US Patent App. 14/891353 (2014).

[5] A. F. O. Falcão, L. M. C. Gato, J. C. C. Henriques, J. E. Borges, B. Pereiras, F. Castro, A novel twin-rotor radial-inflow air turbine for oscillating-water-column wave energy converters, Energy 93, (2015) 2116–2125, https://doi.org/10.1016/j.energy.2015.10.046.

[6] J. E. Borges, Three-dimensional design of turbomachinery, Ph.D. thesis, UK: University of Cambridge (1986).

[7] J. T. Q. Melo, Projeto do difusor de uma turbina tetra-radial auto-retificadora, Master's thesis, Universidade de Lisboa, Instituto Superior Técnico (2016).

[8] J. P. Holman, Experimental methods for engineers, McGraw-Hill, 2001.

[9] A. F. O. Falcão, R. J. A. Rodrigues, Stochastic modelling of OWC wave power plant performance, Appl Ocean Res 24 (2) (2002) 59–71, http://dx.doi.org/10.1016/ S0141-1187(02)00022-6.

[10] J. S. Alves, Experimental and CFD analysis of a biplane wells turbine for wave energy harnessing, Master's thesis, KTH, School of Engineering Sciences (2013).